PCCP

PAPER

View Article Online
View Journal

Cite this: DOI: 10.1039/c7cp05105k

Correlation between the structural change and the electrical transport properties of indium nitride under high pressure†

HPSTAR 454-2017

Junkai Zhang,[ab] Ji Qi,[a] Yanzhang Ma,[c] Tingjing Hu,[a] Jiejuan Yan,[d] Feng Ke,[d] Xiaoyan Cui,[a] Yang Gao,[c] Meiling Sun*[be] and Chunxiao Gao*[b]

Received 28th July 2017,
Accepted 6th September 2017

DOI: 10.1039/c7cp05105k

rsc.li/pccp

We report on the intriguing structural and electrical transport properties of compressed InN. Pronounced anomalies of the resistivity, Hall coefficient, electron concentration, and mobility are observed at ~11.5 GPa, accompanied by a wurtzite–rocksalt structural transition confirmed using high-pressure XRD measurements and first-principles calculations. The pressure-tuned electrical properties of wurtzite and rocksalt InN are also studied, respectively. Particularly, compression pressure significantly decreases the electron concentration of rocksalt InN by two orders of magnitude and increases the mobility by ten fold. The obvious variations in electrical parameters can be rationalized by our band structure simulations, which reveal a direct–indirect energy crossover at 10 GPa, followed by the rapidly increasing patterns of the energy gap with a pressure coefficient of 33 meV GPa^{-1}. Moreover the electron effective mass and energy gap are found to well satisfy with the $k\cdot p$ model. Definite correlation between the structural change and the electrical transport properties should shed a new light on building InN-based applications in the future.

1. Introduction

Indium nitride (InN) usually crystallizes in the wurtzite phase (w-InN, space group $P63mc$) under ambient conditions,[1] exhibiting better physical properties including the highest mobility, electronic drift velocity, peak drift velocity, and the lowest electron effective mass among the group-III nitride semiconductor materials. Thus InN shows significant applications in high-frequency, high-speed electronic devices,[2,3] and THz emission.[4,5] Furthermore, by varying the composition of quaternary (InAlGa)N alloys, the energy gap (E_g) can be tuned over a wide spectral range from near-infrared to ultraviolet, which hints at the potential application of InN in high-efficiency solar cells, light emitting diodes, and large-aperture photoconductive antennas.[6,7] However, a further improvement in the quality of InN samples (*e.g.*, surface roughness and charge carrier concentration) is needed. Considerable efforts have been made to enhance the electrical and optical properties of InN by morphological variations including nanorods, nanowires, and size-confined nanobelts, *etc.*[8,9]

High pressure has been shown to be a powerful factor in modulating the crystallographic and electronic structures of materials. Pioneering studies illustrated that both electrical parameters and energy gaps can be tuned significantly in compound semiconductors by compression,[10,11] which provides a new possible route for modulating the physical properties of InN.

Under high pressure, Ueno *et al.* have carried out X-ray diffraction (XRD) studies on InN, and proposed that InN went through a structural transition from the wurtzite phase to the rocksalt phase (c-InN, space group $Fm\bar{3}m$) at about 12.1 GPa.[12] Subsequently, Pinquier *et al.* conducted Raman spectral measurements to state that w-InN went through a gradual transition starting from 11.6 GPa and fully transformed into the rocksalt structure above 13.5 GPa.[13,14] Over the following years, many groups confirmed the wurtzite–rocksalt structural transition by means of XRD spectra, Raman scattering, and infrared reflectance techniques, *etc.*[15–17] Alternatively, theoretical studies on InN were also conducted to discuss the electronic structure and compressibility of both phases.[18–21] Despite the fact that great

---

[a] Key Laboratory of Functional Materials Physics and Chemistry of the Ministry of Education, Jilin Normal University, Siping, 136000, China

[b] State Key Laboratory of Superhard Materials, Jilin University, Changchun, 130012, China. E-mail: cc060109@qq.com

[c] Department of Mechanical Engineering, Texas Tech University, Lubbock, TX 79409, USA

[d] Center for High Pressure Science and Technology Advanced Research, Shanghai, 201203, China

[e] School of Physics and Optoelectronic Engineering, Shandong University of Technology, Zibo, 255000, China. E-mail: sunml@sdut.edu.cn

† Electronic supplementary information (ESI) available: Values of E_g and dE_g/dP for the different candidate phases of InN and the phase transition pressures. See DOI: 10.1039/c7cp05105k

efforts have been made in studying the crystal and electronic structures of InN under pressure, it remains unexplored how the compression tunes electrical parameters necessary for InN-based applications, including the resistivity (ρ), Hall coefficient (R_H), charge carrier concentration (n), and mobility (μ), *etc.* Moreover, much work is still needed to establish the correlation between the structural change and the electrical transport properties, the lack of which precludes further understanding of the kinds of nitride functional materials.

Motivated by the above mentioned issues, we conducted high-pressure *in situ* synchrotron X-ray diffraction and electrical measurements on InN combining theoretical simulations. XRD spectra were recorded to monitor the structural modification, which is still not well-defined but of great importance for understanding the changes in the physical properties of InN under compression. In addition, resistivity and Hall-effect measurements were adopted to study the pressure-induced modulation of electrical parameters. First-principles calculations were applied to illustrate the structural transition mechanism and band structure details, and then rationalize the variations in the electrical transport properties under compression.

2. Experimental and computational details

Polycrystalline InN powder bought from Alfa Aesar Co. with a stated purity of 99.9% was used as the sample. X-ray diffraction data for powder samples under ambient conditions were collected using a RIGAKU diffractometer with monochromatic Cu-Kα radiation, and the patterns show better agreement with the wurtzite phase (JCPDS file No. 50-1239) (Fig. 1(a)). High pressure was generated using a nonmagnetic diamond anvil cell (DAC) with an anvil culet of 300 μm in diameter. A nonmagnetic rhenium flake used as the gasket was indented to $\sim$50 μm in thickness. A hole with 200 μm in diameter was drilled in the center of the indentation using a laser. Then, a mixture of alumina powder and epoxy was inserted and compressed into the hole as the insulating layer. Subsequently, another hole with 150 μm was drilled and served as a sample chamber. The thickness of the sample under pressure was determined using a micrometer with a precision of 0.5 μm, and the deformation of diamond anvils was taken into account.[22] No pressure medium was loaded in order to avoid additional errors in electrical measurements. The ruby fluorescence method was used for the pressure calibration. van der Pauw configuration electrodes were integrated on the diamond surface. The fabrication method of probing a microcircuit on diamond has been reported previously.[22–25] Fig. 1(b) and (c) show the microcircuit and the sectional view of DAC to illustrate the sample loading method.

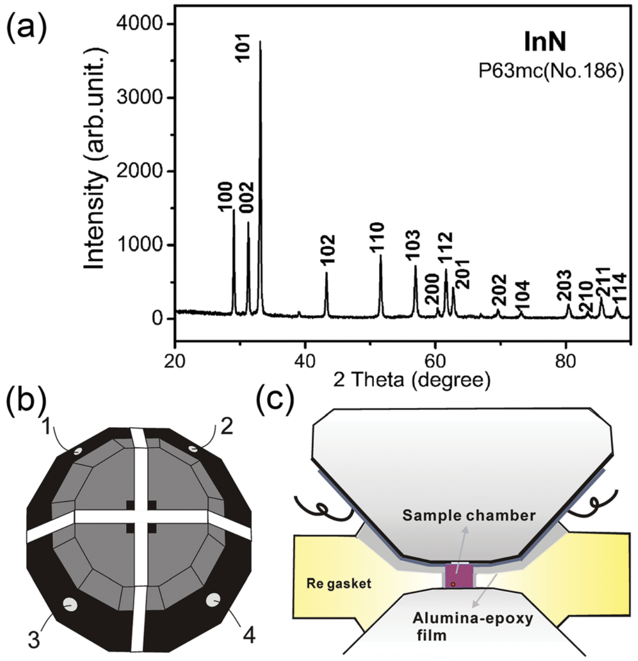

Fig. 1 (a) X-ray diffraction patterns of InN under ambient conditions. (b) Configuration of a microcircuit on a diamond anvil. Here 1, 2, 3, and 4 are the silver wires. (c) Cross section of the designed DAC.

In situ resistivity and Hall-effect measurements under high pressure were conducted using the current reversal method to avoid thermoelectric offsets. The current, typically 100 mA, was sourced by a Keithley 2400 Source Meter and the voltage was measured using a Keithley 2700 Multimeter. All instruments were connected to a computer *via* a Keithley Kusb-488 interface adapter and a general purpose interface bus. The measurement process was automatically performed using the van der Pauw method. Hall-effect measurements were carried out in a magnetic field of 1.5 T.

In situ high-pressure XRD experiments were conducted at the Beamline X17C of the National Synchrotron Light Source (NSLS) using an angle-dispersive XRD source (λ = 0.406750 Å). A methanol–ethanol–water (16 : 3 : 1) mixture was used as the pressure transmitting medium. The experimental parameters including the distance between the sample and detector were calibrated using the CeO_2 standard materials. Bragg diffraction images were integrated using FIT2D software to obtain intensity *versus* diffraction angle 2θ patterns. XRD patterns were fitted using the GSAS program package.[26]

First-principles calculations were conducted using the density functional theory (DFT) and pseudopotential method.[27] Electronic structures were simulated using the CASTEP code inserted in Materials Studio.[28] The electron–ion interaction was described using the Vanderbilt-type ultrasoft pseudopotential.[29] The exchange and correlation terms were described by generalized gradient approximations (GGAs) in the scheme of Perdew–Burke–Ernzerhof (PBE) parameterization.[30] The geometric optimization of the unit cell was carried out using the BFGS minimization algorithm.[28] The configurations of In and N were $4d^{10}5s^25p^1$ and $2s^22p^3$, respectively. Convergence of the total energy was checked with respect to both plane wave cutoff energy and k-point density, which were obtained using the Monkhorst–Pack method.[31] The one-electron valence state was expanded on a plane wave basis with a cutoff energy of 500 eV. Integration in the Brillouin zone was performed using special k points generated with 11 × 11 × 6 and 13 × 13 × 13 mesh parameter grids for wurtzite and rocksalt InN, respectively.

The chosen plane-wave cutoff energy and the number of k points were carefully checked to ensure that the total energy converged to better than 1 meV per atom. The space group of wurtzite InN was $P63mc$ (No. 186) at 0 GPa with calculated lattice parameters $a = b = 3.52$ Å, $c = 5.7024$ Å, and one internal parameter $u = 0.375$[19] and the space group of rocksalt InN was $Fm\bar{3}m$ (No. 225) at 11 GPa with calculated lattice parameters $a = b = c = 4.63$ Å.[19] The relative stability of different structural phases is examined by comparing their enthalpy values.

3. Results and discussion

XRD measurements were carried out to monitor the structural modification of InN under compression. Fig. 2(a) shows the selected XRD patterns of InN at various pressures. At ambient pressure, the pattern of InN can be well indexed into the wurtzite ($P63mc$) structure as in the previously reported results.[1] It is found that, upon gradually increasing the pressure up to 12.9 GPa, new diffraction peaks at ∼10.25° suddenly emerge, which clearly signals the starting of wurtzite–rocksalt structural transition. With further compression of up to 16.7 GPa, other three new diffraction peaks gradually appear at ∼14.52°, ∼17.06°, and ∼17.82°. Above 23.8 GPa, the transformation is complete and no further transition is observed up to 30.8 GPa, the highest pressure in this work. The structural transition is found to be reversible. After the release of full pressure, InN recovers to the ambient-pressure wurtzite structure. As shown in Fig. 2(b) the patterns of c-InN can be indexed into the rocksalt structure. The lattice parameters at 16.7 GPa are refined to $a = b = c = 4.55$ Å.

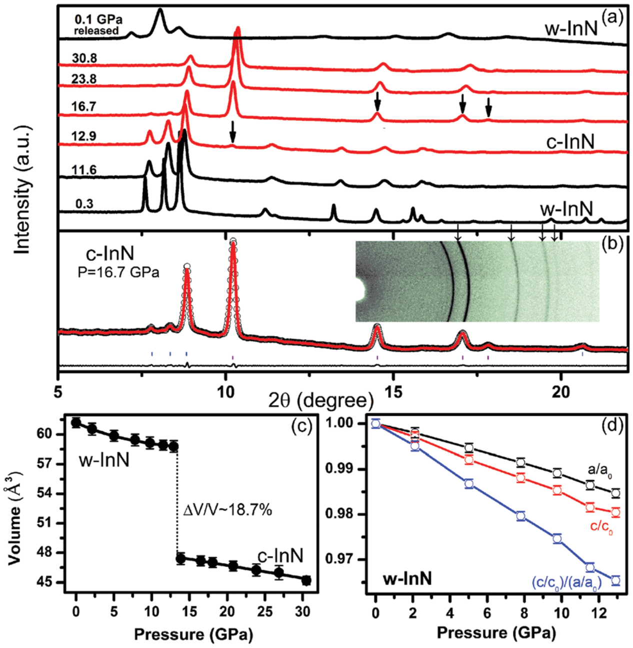

Fig. 2 (a) Representative XRD patterns of InN at various pressures. (b) Rietveld refinement of c-InN at 16.7 GPa (R_w = 1.62% and R_{wp} = 4.21%). (c) Volume *versus* pressure curve of w-InN and c-InN obtained using XRD and geometry optimization. (d) Lattice parameters as a function of pressure for w-InN.

The structural transition is accompanied by a pronounced volume collapse of ∼18.7%. The compressibility of the c/a ratio in w-InN is found to be approximately linear without any anomaly before the structural transition (Fig. 2(d)).

A discontinuous change in the electrical transport properties usually coincides with crystal structural transition. As shown in Fig. 3, the original value of ρ is 2.5×10^{-3} Ω cm under ambient conditions, and the ρ–P curves of InN can be divided into three stages of I′, I, and II as 0–4.4 GPa, 4.4–11.5 GPa, and 11.5–22.0 GPa, respectively. Stage I′ is mainly attributed to the reduction of particle gaps and the recombination of grains under low compression. In stage I, ρ increases smoothly with pressure elevation. At 11.5 GPa, a pronounced variation is that ρ changes its pressure dependence and increases rapidly with pressure up to 22.0 GPa, which is the cause of the wurtzite–rocksalt structural transition of InN and further the increase of the energy gap in c-InN (more details can be found in band structure calculations). Remarkably, it is unusual that ρ increases continuously with pressure after the pressure-induced structural transition, which probably supplies the potential applications for InN materials and excites our further research interests. Under decompression, ρ decreases smoothly upon quenching to ambient pressure, and does not return back to its original value.

To further study the charge carrier transportation of InN under compression, the pressure dependencies of R_H, n, and μ were examined by *in situ* Hall-effect measurements, as shown in Fig. 4. Under ambient conditions, R_H, n, and μ are -3.6×10^{-2} cm^3 C^{-1}, 2.0×10^{20} cm^{-3}, and 63.0 cm^2 V^{-1} s^{-1}, respectively.

At low compression pressure (around a few GPa), the uncontrolled particle gaps in the InN sample usually can be considered as potential barriers and heavily hinder the transportation of charge carriers. These types of particle gaps should be significantly decreased with loading pressure and lead to an increase in n and a decrease in μ. From 1.5 GPa to 4.4 GPa, further compression turns to drive the recombination of grains in the sample, which indicates that the atoms among grains

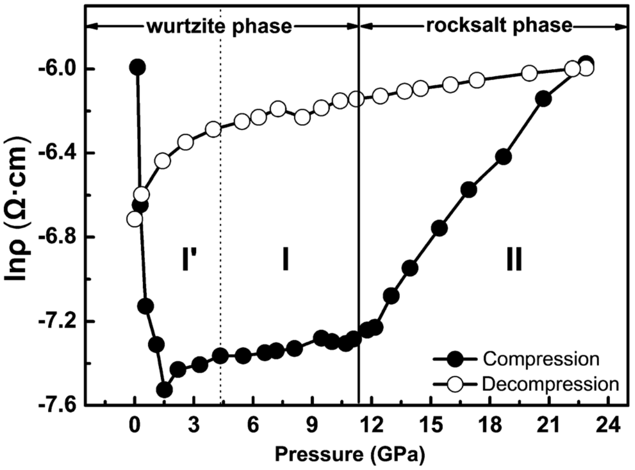

Fig. 3 Pressure dependent resistivity (ρ) of InN at room temperature. I′, I, and II are assigned to three stages (I′ and I represent the wurtzite phase; II is the rocksalt phase).

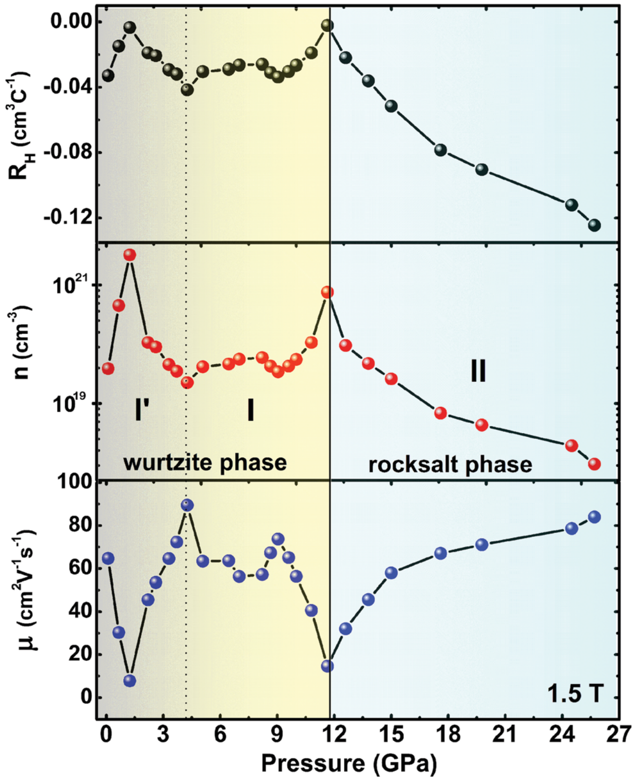

Fig. 4 Pressure dependent Hall coefficient (R_H), charge carrier concentration (n), and mobility (μ) of InN at room temperature. Pressure range is also assigned to three stages as I′, I, and II, consistent with the ρ–P curves.

undergo a rearrangement transition from disordered to a relatively stable and ordered state.[32–36] New chemical bonds should be rebuilt between adjacent atoms nearby grains with the decrease of the inter-atomic distance. Hence, the dangling bonds tend to reduce with pressure, leading to the reduction of the defect concentration. The above factors result in the decrease of n and the increase of μ from 1.5 to 4.4 GPa.

Before and after 11.5 GPa, it is obviously found that the wurtzite–rocksalt structural transition of InN results in a series of discontinuous changes in R_H, n, and μ, which are attributed to a comprehensive contribution of the variations in both crystal periodical vibrations and band structures during the transition. In w-InN, the decreased mobility is almost completely compensated by the increased charge carrier concentration, which is considered as the cause of slightly increased resistivity below 11.5 GPa. In c-InN, n decreases continuously with pressure elevation because of the broadening of the energy gap, in turn, will reduce the electron scattering probability and increase the electron mean free time. Therefore, μ is found to increase synchronously. Such a phenomenon probably extends to a higher pressure. Backwards, the pressure tuned modulation for w-InN is also checked, which makes n and μ achieve the minimum and maximum value at 4.4 GPa, respectively. The above factors, ideally, affect the ability of InN materials to exhibit higher THz emission and better optoelectronic properties,[3–6] and provide a new idea of high-temperature high-pressure (HTHP) synthesis on different phases of InN with excellent stability and good performance.

It is possible to investigate the subtle variations in electrical parameters during the phase transition using electrical measurements. However, it is insufficient if what we really want to do is to discuss the possible correlation between the phase structure and charge carrier transportation. We need access to the first-principles calculations for the purpose of exploring the mechanism behind structural transition and rationalizing the anomalous variations in the electrical transport properties.

The calculated enthalpy curve (relative to w-InN) confirms the energetic stability of the high-pressure rocksalt structure of InN. Above 10 GPa, the rocksalt phase is more stable, in agreement with our XRD observations (Fig. 5(a)). A large volume collapse of ~17.8% is also found to significantly reproduce the experimental data. Phonon calculations establish the dynamical stabilities of the calculated rocksalt structure in view of the absence of imaginary frequencies (Fig. 5(b)). Above structural transformation derives from the significant reduction of the bonding angle of the nitrogen–indium bonds In(1)–N–In(2) and the decrease of the mean distance of two indium atoms along the c-axis (In1) and the off-axis (In2) (Fig. 5(c)),[37] which drive the transition into a rocksalt structure, where the In1–N–In2 angle decreases to 90°. The lattice rebuilding will modify the electronic structures of c-InN, and hence, bring about many significant variations in electrical parameters (Table 1).

Fig. 6 summarizes the energy gap *versus* pressure of InN obtained from the band structure calculations. In w-InN at 0 GPa, the valence-band maximum (VBM) and the conduction-band minimum (CBM) are both located at the G point. The energy gap between the VBM and CBM is found to be very low positive, E_g ~ 0.08 eV, which can be attributed to an over-estimation of 'GGA or LDA error' for pd repulsion[41–43] and hence, of the shift of the VBM towards higher energies.

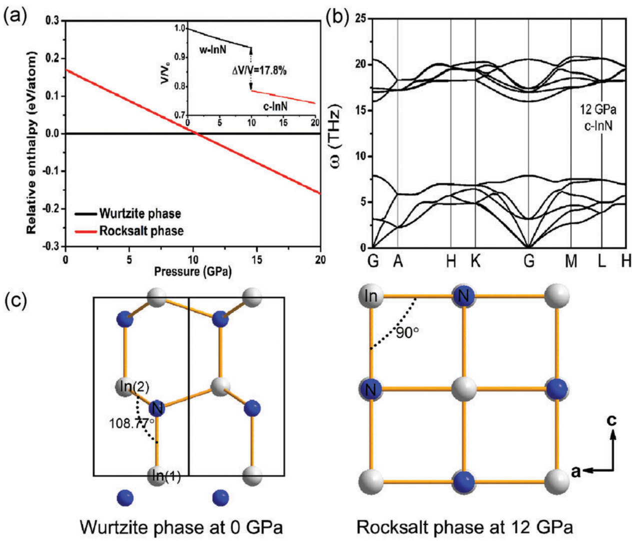

Fig. 5 (a) Enthalpy curve (relative to w-InN) of c-InN as a function of pressure. Enthalpies are given per atom. Inset is calculated volume *versus* pressure data. (b) Phonon spectrum distribution of c-InN at 12 GPa. (c) Polyhedral views of InN in the wurtzite phase at 0 GPa and the rocksalt phase at 12 GPa, respectively.

Table 1 Pressure dependent E_g and $\ln\rho$ for the wurtzite and the rocksalt phase of InN, respectively

Phase	Pressure stage (GPa)	$(2k_BT)^{-1}$ dE_g/dP (GPa^{-1}) (theoretical)	Error (%)	d($\ln\rho$)/dP (GPa^{-1}) (experimental)	Error (%)
Wurtzite	4.4–11.5	0.018	3.19	0.023	5.45
Rocksalt	11.5–26.1	0.482	2.86	0.513	4.02

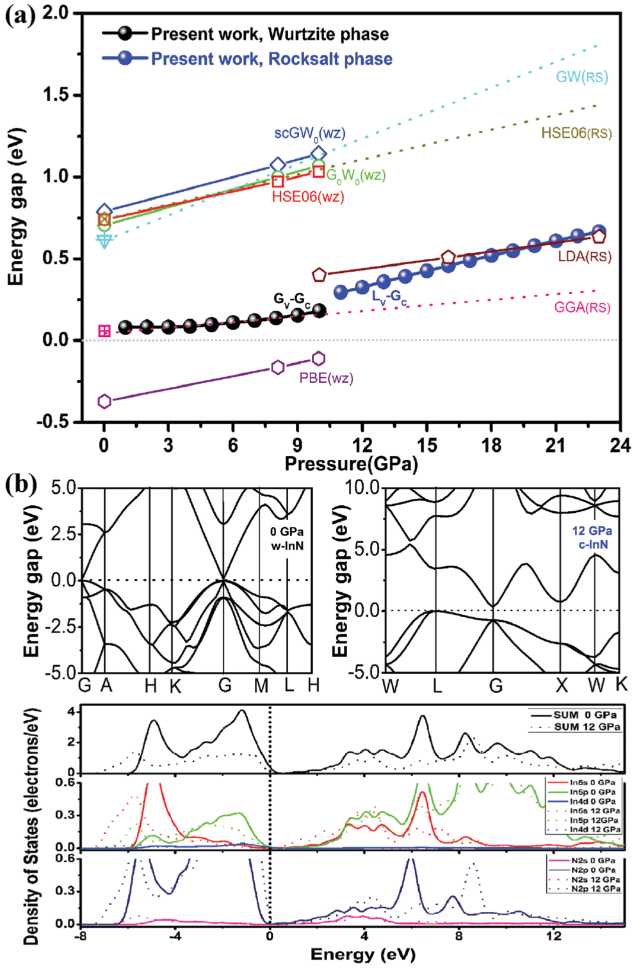

Fig. 6 (a) Pressure dependent energy gap (E_g) of InN. The solid spheres are this work; the empty symbols from ref. 38–40. (b) The top half represents the band structures in w-InN at 0 GPa and c-InN at 12 GPa along with the selected high-symmetry lines, respectively. The bottom half is the corresponding total and partial density of states at 0 GPa and 12 GPa.

Nevertheless, it has been well established that pressure derivatives of E_g calculated within the same framework are worth learning.[44–47] Meanwhile, to guarantee the accuracy of E_g at different pressures, we checked the energy gap at various levels of theory where the HSE and GW methods were adopted for comparison, as shown in Fig. 6(a) (see more details in the ESI†). From this it is found that E_g of w-InN increases smoothly with increasing pressure, and then the VBM shifts from the G point to the L point at 10 GPa followed by the wurtzite–rocksalt structural transition, which indicates that pressure realizes the direct–indirect crossover of the energy gap of InN. Above 10 GPa, E_g of c-InN shows a sharp increase and continues to increase with a pressure coefficient of 33 meV GPa^{-1}, which is the result of the movement of the CBM away from the VBM caused by the enhancement of hybridization between the In 5p-orbit and the N 2p-orbit with pressure elevation (the bottom half of Fig. 6(b)).

In the intrinsic range the resistivity of semiconductors can be represented by the following formula: $\rho = \rho_0 \exp[E_g/2k_BT]$, where ρ_0 is constant that is approximately independent of pressure as compared with the exponential term, E_g. And ρ is the resistivity, k_B is the Boltzmann constant, T represents the temperature.[48–50] In this work, we also examined dE_g/dP obtained from band structure calculations and d($\ln\rho$)/dP obtained from resistivity measurements in both wurtzite and rocksalt phases, respectively. Taking no account of the errors from the thickness measurement and the fitting procedure, it can be found that dE_g/dP and d($\ln\rho$)/dP satisfy the Arrhenius relationship better as given by eqn (1) when C is predefined as 1.

$$\mathrm{d}(\ln\rho)/\mathrm{d}P = (C/2k_BT)(\mathrm{d}E_g/\mathrm{d}P) \quad (1)$$

where C is constant for the purposes of revision control and is affected by different calculating methods. These results clearly indicate that the increased resistivity of InN can be seen as a consequence of the energy gap broadening.

In our Hall-effect measurements, InN shows the priority to electron conduction below 26.8 GPa at room temperature. In fact, InN is one of the representatives for a n-type extrinsic semiconductor. Almost all electrons participating in the conduction are from the donor ionization rather than the intrinsic excitation. Thus, the electron concentration of InN approximately equals to the ionized donor concentration (N_i), *i.e.*, $n \approx N_i$. On the other hand, the mobility is mainly controlled by the donor scattering, which is defined by eqn (2),

$$\mu = \mu_n = q\tau_n/m_n{}^* \quad (2)$$

where μ_n refers to the electron mobility, q is the electron charge absolute value, τ_n is the electron mean free time, $m_n{}^*$ is the electron effective mass. Besides, $\tau_n \propto N_i{}^{-1} \approx n^{-1}$. Thus, the resistivity can be proportional to the electron effective mass as a whole, which is calculated using eqn (3),

$$\rho = 1/nq\mu = m_n{}^*/nq^2\tau_n \propto m_n{}^* \quad (3)$$

Moreover, the electron effective mass can be calculated from band structures with eqn (4),

$$m_n{}^*/m_0 = \hbar^2/(\mathrm{d}^2E/\mathrm{d}k^2)_{k=k\,\mathrm{min}}/m_0 \quad (4)$$

where m_0 is the free electron mass.

Fig. 7 indicates that the electron effective mass is basically proportional to the energy gap of InN, consistent with the $k{\cdot}p$ model.[51] Combined with the results of eqn (3), it is clearly shown that the electron effective mass is one of the critical factors to make the energy gap of InN coincide with experimental resistivity.

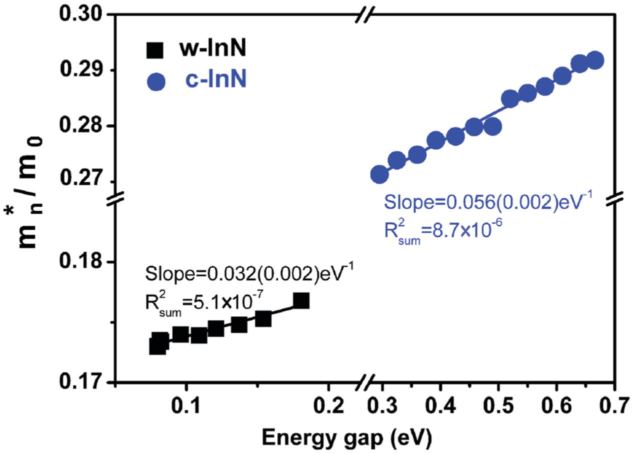

Fig. 7 Energy gap dependent electron effective mass of InN. R_{sum}^2 indicates the residual sum of squares about the linear fitting results.

The increase of the energy gap directly causes the increase of resistivity. Band structure calculations conclude a good agreement with the results of the electrical transport properties, beneficial for building InN-based applications in the future.

4. Conclusions

In summary, the accurate high-pressure *in situ* XRD, resistivity, Hall-effect measurements and first-principles calculations were carried out on InN. We observed a series of abnormal electrical responses to the pressure driven wurtzite–rocksalt structural transition around 11.5 GPa, and found that compression pressure produces a decrease of the electron concentration and an increase of mobility, and hence finishes modulates the electrical performance of wurtzite and rocksalt InN, respectively. Furthermore, first-principles calculations revealed the variation mechanism of electronic and crystal structures induced by compression. Band structure simulations show that the energy gap increases with pressure elevation and that there is a significant direct–indirect gap transformation at 10 GPa. Meanwhile the calculated electron effective mass and energy gap were found to well satisfy with the *k·p* model. Above calculations rationalized the anomalous variations in electrical parameters in the full pressure range and built the correlation between the structural change and the electrical transport properties. Our results reported here should raise the hopes of InN material-based optoelectronics with high performances and good stability.

Conflicts of interest

There are no conflicts to declare.

Acknowledgements

This work was supported by the National Natural Science Foundation of China (Grant No. 11304034, 11374121, 11404133, 11404137, 61378085, 21776110, and 51608226) and the Twentieth Five-Year Program for Science and Technology of Education Department of Jilin Province (Item No. 20150221).

References

1 D. Fritsch, H. Schmidt and M. Grundmann, *Phys. Rev. B: Condens. Matter Mater. Phys.*, 2003, **67**, 235205.
2 P. Wei, W. Z. Shen, H. Ogawa and Q. X. Guo, *Phys. Rev. B: Condens. Matter Mater. Phys.*, 2004, **24**, 195.
3 S. A. Shevlin, Z. X. Guo, H. J. J. van Dam, P. Sherwood, C. R. A. Catlow, A. A. Sokol and S. M. Woodleyc, *Phys. Chem. Chem. Phys.*, 2008, **10**, 1944.
4 R. Ascázubi, I. Wilke, K. Denniston, H. Lu and W. J. Schaff, *Appl. Phys. Lett.*, 2004, **84**, 4810.
5 G. Matthäus, V. Cimalla, B. Pradarutti, S. Riehemann, G. Notni, V. Lebedev, O. Ambacher, S. Nolte and A. Tünnermann, *Opt. Commun.*, 2008, **14**, 3776.
6 T. C. Shibin Krishna and G. Gupta, *RSC Adv.*, 2014, **4**, 27308.
7 A. Eljarrat, L. López-Conesa, C. Magén, N. García-Lepetit, Ž. Gačević, E. Calleja, F. Peiró and S. Estradé, *Phys. Chem. Chem. Phys.*, 2016, **18**, 23264.
8 Q. Yang, Y. P. Wu, Y. Liu, C. F. Pan and Z. L. Wang, *Phys. Chem. Chem. Phys.*, 2014, **16**, 2790.
9 G. G. Wu, W. T. Zheng, F. B. Gao, H. Yang, Y. Zhao, J. Z. Yin, W. Zheng, W. C. Li, B. L. Zhang and G. T. Du, *Phys. Chem. Chem. Phys.*, 2016, **18**, 20812.
10 X. Zhang, J. K. Zhang, F. Ke, G. H. Li, Y. M. Ma, X. Z. Liu, C. L. Liu, Y. H. Han, Y. Z. Ma and C. X. Gao, *RSC Adv.*, 2015, **5**, 54843.
11 J. J. Yan, F. Ke, C. L. Liu, L. Wang, Q. L. Wang, J. K. Zhang, G. H. Li, Y. H. Han, Y. Z. Ma and C. X. Gao, *Phys. Chem. Chem. Phys.*, 2016, **18**, 5012.
12 M. Ueno, M. Yoshida, A. Onodera, O. Shimomura and K. Takemura, *Phys. Rev. B: Condens. Matter Mater. Phys.*, 1994, **49**, 14.
13 C. Pinquier, F. Demangeot, J. Frandon, J. Pomeroy, M. Kuball, H. Hubel, N. Van Uden, D. Dunstan, O. Briot and B. Maleyre, *Phys. Rev. B: Condens. Matter Mater. Phys.*, 2004, **70**, 113202.
14 C. Pinquier, F. Demangeot, J. Frandon, J. C. Chervin, A. Polian, B. Couzinet, P. Munsch, O. Briot, S. Ruffenach and B. Gil, *Phys. Rev. B: Condens. Matter Mater. Phys.*, 2006, **73**, 115211.
15 Q. Xia, H. Xia and A. L. Ruoff, *Mod. Phys. Lett. B*, 1994, **8**, 345.
16 L. D. Yao, S. D. Luo, X. Shen, S. J. You, L. X. Yang and S. J. Zhang, *J. Mater. Res.*, 2010, **25**, 2330.
17 R. Oliva, A. Segura, J. Ibáñez, T. Yamaguchi, Y. Nanishi and L. Artús, *Appl. Phys. Lett.*, 2014, **105**, 232111.
18 J. Serrano, A. Rubio, E. Hernández, A. Muńoz and A. Mujica, *Phys. Rev. B: Condens. Matter Mater. Phys.*, 2000, **62**, 16612.
19 S. Saib and N. Bouarissa, *Phys. B*, 2007, **387**, 377.
20 F. Peng, Y. Han, H. Fu and X. Cheng, *Phys. Status Solidi B*, 2008, **245**, 2743.

21 J. M. Panchal, M. Joshi and P. N. Gajjar, *Phase Transitions*, 2016, **89**, 1.

22 C. Gao, Y. Han, Y. Ma, A. White, H. Liu, J. Luo, M. Li, C. He, A. Hao and X. Huang, *Rev. Sci. Instrum.*, 2005, **76**, 083912.

23 M. Li, C. Gao, Y. Ma, Y. Li, X. Li, H. Li, J. Liu, A. Hao, C. He and X. Huang, *Rev. Sci. Instrum.*, 2006, **77**, 123902.

24 M. Li, C. Gao, Y. Ma, D. Wang, Y. Li and J. Liu, *Appl. Phys. Lett.*, 2007, **90**, 113507.

25 J. J. Yan, F. Ke, C. L. Liu, Q. L. Wang, J. K. Zhang, L. Wang, G. Peng, Y. H. Han, Y. Z. Ma and C. X. Gao, *Phys. Chem. Chem. Phys.*, 2015, **17**, 26277.

26 A. C. Larson and R. B. Von Dreele, *General Structure Analysis System (GSAS) LAUR*, Los Alamos National Laboratory, New Mexico, 2004.

27 S. Baroni, P. Giannozzi and A. Testa, *Phys. Rev. Lett.*, 1987, **58**, 1861.

28 T. H. Fischer and J. Almlof, *J. Phys. Chem.*, 1992, **96**, 9768.

29 D. Vanderbilt, *Phys. Rev. B: Condens. Matter Mater. Phys.*, 1998, **41**, 7892.

30 J. P. Perdew, K. Burke and M. Ernzerhof, *Phys. Rev. Lett.*, 1996, **77**, 3865.

31 H. J. Monkhorst and J. D. Pack, *Phys. Rev. B: Solid State*, 1976, **13**, 5188.

32 M. B. Omri, J. P. Michel and A. George, *Philos. Mag. A*, 1990, **62**, 203.

33 S. Edmiston, G. Heiser, A. Sproul and M. Green, *J. Appl. Phys.*, 1996, **80**, 6783.

34 Y. Yan, M. Chisholm, G. Duscher, A. Maiti, S. Pennycook and S. Pantelides, *Phys. Rev. Lett.*, 1998, **81**, 3675.

35 S. Kodiyalam, R. K. Kalia, H. Kikuchi, A. Nakano, F. Shimojo and P. Vashishta, *Phys. Rev. Lett.*, 2001, **86**, 55.

36 Y. Li, Y. Han, Y. Ma, P. Zhu, X. Wang and C. Gao, *Europhys. Lett.*, 2012, **98**, 66006.

37 L. Bellaiche, K. Kunc and J. Besson, *Phys. Rev. B: Condens. Matter Mater. Phys.*, 1996, **54**, 8945.

38 W. X. Feng, S. X. Cui, H. Q. Hu and W. Zhao, *Phys. Status Solidi B*, 2010, **247**, 313–317.

39 Y. F. Duan, L. X. Qin, L. W. Shi and G. Tang, *Comput. Mater. Sci.*, 2015, **101**, 56–61.

40 A. M. Alvarado, High-Pressure, Properties of Several Narrow Band gap Semiconductors from First-Principles Calculations, 2016, *UNLV Theses*, *Dissertations*, *Professional Papers, and Capstones*. 2629.

41 M. S. Hybertsen and S. G. Louie, *Phys. Rev. B: Condens. Matter Mater. Phys.*, 1986, **34**, 5390.

42 S. H. Wei and A. Zunger, *Phys. Rev. B: Condens. Matter Mater. Phys.*, 1988, **37**, 8958.

43 F. Bechstedt, *Adv. Solid State Phys.*, 1992, **32**, 161.

44 V. Fiorentini, *Phys. Rev. B: Condens. Matter Mater. Phys.*, 1992, **46**, 2086–2091.

45 C. J. Wu, L. H. Yang, L. E. Fried, J. Quenneville and T. J. Martinez, *Phys. Rev. B: Condens. Matter Mater. Phys.*, 2003, **67**, 235101.

46 F. Ke, J. Yang, C. L. Liu, Q. L. Wang, Y. Q. Li, J. K. Zhang, L. Wu, X. Zhang, Y. H. Han, B. J. Wu, Y. Z. Ma and C. X. Gao, *J. Phys. Chem. C*, 2013, **117**, 6033–6038.

47 J. J. Yan, F. Ke, C. L. Liu, L. Wang, Q. L. Wang, J. K. Zhang, G. H. Li, Y. H. Han, Y. Z. Ma and C. X. Gao, *Phys. Chem. Chem. Phys.*, 2016, **18**, 5012–5018.

48 J. Bardeen and W. Shockley, *Phys. Rev.*, 1950, **80**, 72–80.

49 Y. Akahama, S. Endo and S. Narita, *Physica B+C*, 1986, **139**, 397–400.

50 J. Z. Jiang, L. Gerward, R. Secco, D. Frost, J. S. Olsen and J. Truckenbrodt, *J. Appl. Phys.*, 2000, **87**, 2658–2660.

51 E. Kane, *Semicond. Semimetals*, 1966, **1**, 75.